

CFD Analysis of a Re-Usable First Stage in the Transonic Regime

Tamás Bykerk^{1*}, Tim Horchler¹

¹ The German Aerospace Center, Bunsenstr. 10, Göttingen, 37073, Germany

*Emailto: tamas.bykerk@dlr.de

Abstract

This paper presents drag coefficient and unsteady pressure loads for the RFZ model in the transonic regime. The RFZ model is an open-source, common research geometry for re-usable launchers and is used as tool for the space community to benchmark aerodynamic and aerothermal results. This work addresses a gap in the current literature, where no detailed information on re-usable orbital class launchers during the transonic regime of the return to earth phase of flight exists. Numerical simulations using steady-state Reynolds Averaged Navier Stokes, as well as unsteady improved Delayed Detached Eddy Simulations have been completed. Results show that the trend for drag coefficient agrees well with published results for a cylinder placed in an axial flow, where drag is mostly attributed to the high pressure on the surface of the baseplate and the nozzles. Flow separation off the nozzles influences the local flowfield experienced by the landing leg covers, but predominantly affects the pressure loads recorded on the baseplate. Future work will extend this study to include the effect of a single active engine at Mach 0.75, indicative of the landing burn, as well as determine if unsteady loads in the vehicle base area pose any risk of structural excitation.

1 Introduction

Aeronautical engineers have a long history of developing standardized models for wind tunnel calibrations and data comparisons between facilities. They are extremely useful in providing baseline datasets for correlation of results, data repeatability over time and verifying model installation or data acquisition systems. Reference models are also particularly relevant from the perspective of numerical analyses, where different codes can be directly compared with each other or assumptions and solver settings can be experimented with to determine solution sensitivity to certain parameters. A standardized reference model typically fulfills two main criteria. Firstly, they are simplistic in shape with a precisely defined geometry and secondly, they are representative of realistic configurations to ensure that the results are relevant. Examples of existing standard models include the AGARD-B (North Atlantic Treaty Organization, 1958), ONERA-M (Galway and Mokry, 1977) and the Standard Dynamics Model (SDM) (Beyers and Huang, 1990), which have been circulating for decades, while models such as the NASA CRM (Rivers et al., 2015) and the SSAM-Gen5 (Giannelis et al., 2023) provide more up to date and relevant aircraft geometries from the past 10 to 20 years.

Until recently, there has been no reference model for the space community. The RFZ model was developed in response to the sudden and urgent interest in re-usable spacecraft over the past decade (Bykerk, 2023). It serves as a standard test case for the research community to facilitate validation of numerical techniques in the generation of aerodynamic and aerothermal data over the entire trajectory. Since its introduction, work has been conducted on both the first (Karl et al., 2024) and second stage geometries (Basov et al., 2024; Ertl and Bykerk, 2024), with all results made available for public use (Bykerk, 2024).

This paper focuses on expanding the aerodynamic database to include the glide phase for a Mach number range of 0.75 to 1.45. The paper begins with an introduction to the geometry of the RFZ model. This is followed by an overview of the trajectory as well as the test matrix. Next, the numerical setup used for the CFD simulations is outlined, before the results are presented and discussed. Finally, a summary of results and potential avenues for future work is given.

2 RFZ Model

The RFZ model is based on the SpaceX Falcon 9, with the launch, entry and landing configurations presented in Figure 1 below. A comprehensive overview of the design is available in ref. Bykerk (2023), while each of these geometries, as well as the second stage, are available for download in ref. Bykerk (2024). This



paper is concerned with the re-entry configuration, which is characterised by extended planar fins and the lack of second stage (RFZ-REC).

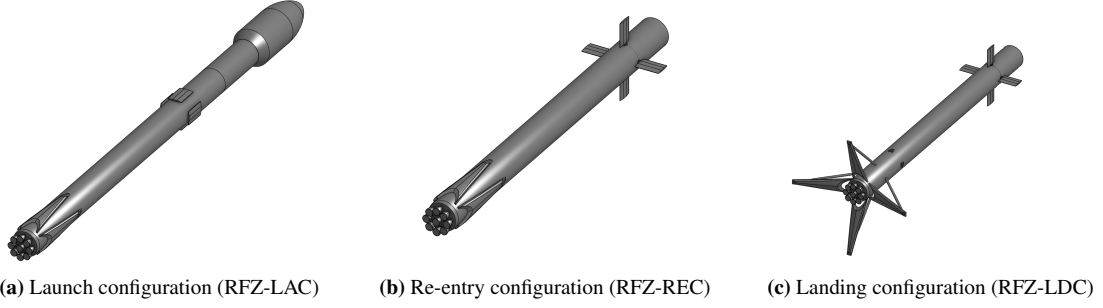


Figure 1. Images showing different views of the RFZ model in various flight configurations.

3 Trajectory and Test Matrix

Re-usable launchers of this type typically follow one of two different trajectory types. The first is a downrange landing, where the first stage is left to follow a natural arc after stage separation and lands away from the launch site. The second is a return to landing site scenario, where following stage separation the first stage alters its trajectory by performing a boost back burn to allow it to land at a designated landing zone close to the launchpad. For both cases the vehicle will complete a re-entry burn, an aerodynamic glide and finally a landing burn. Note that during these phases of flight the vehicle is flying backwards. The work presented in this paper focuses on a downrange landing scenario, with an overview of the trajectory given below in Figure 2 for a low earth orbit (LEO) flight (Bykerk, 2023).

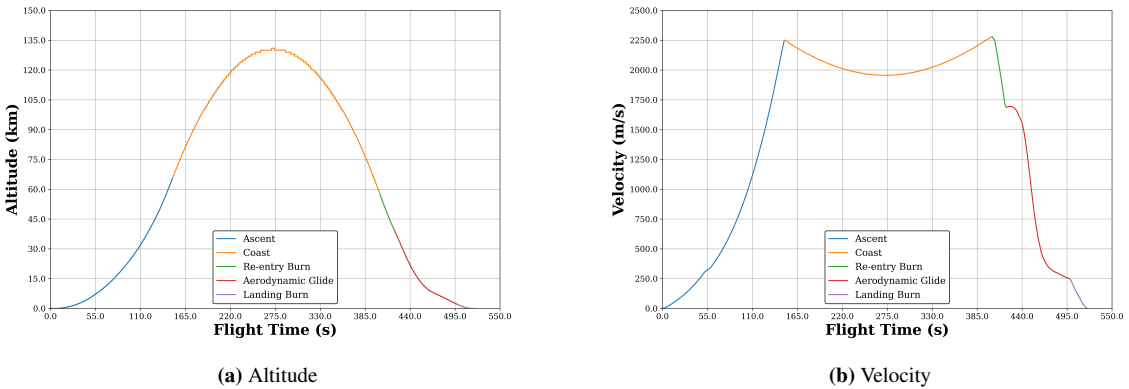


Figure 2. LEO trajectory for the first stage with key events

The vehicle enters the aerodynamic glide phase after the re-entry burn has been terminated at 421 seconds. Between 421 seconds and 498 seconds, the vehicle utilises its control surfaces to guide itself towards a barge located at sea. During this time, the vehicle is exposed to freestream Mach numbers in the range of Mach 5.3 down to Mach 0.75, before the landing burn is commenced. Between 465 and 498 seconds, the vehicle begins to enter the transonic regime and experiences oncoming flow between Mach 1.45 and Mach 0.75. For this investigation, a total of eight trajectory points have been selected to cover this span of Mach numbers (see Table 1). During this time, no engines are active and no control surface deflections or vehicle angle of attack (AoA) is considered.

An additional, high fidelity improved Delayed Eddy Simulation (iDDES) computation is also conducted at the Mach 0.85 trajectory point. The main areas of interest for this simulation are the nozzle extensions and the landing leg covers, whose thin structures may be susceptible to dynamic structural loadings. To aid in solution stability, a small 2 degree AoA has been introduced to prevent the formation of large extended stagnation areas where the flow velocity is close to zero. Furthermore, to reduce the computational expense, the fins have been removed.

Altitude (km)	Velocity (m/s)	Temperature (K)	Pressure (Pa)	Mach Number (-)
8.6	443.5	232.1	32722	1.45
8.3	413.2	234.3	34323	1.35
7.9	386.2	236.9	36286	1.25
7.4	358.7	240.2	39179	1.15
6.6	328.7	245.3	43749	1.05
5.4	302.7	253.2	51624	0.95
3.7	276.7	263.9	63979	0.85
2.0	248.7	275.2	79500	0.75

Table 1. Numerical test matrix for RANS computations.

4 Numerical Setup

The TAU code is a second order finite-volume solver for the Euler and Navier-Stokes equations which includes a comprehensive range of RANS-based or scale resolving turbulence models. It uses unstructured computational grids to facilitate the analysis of complex geometries and is highly optimized for the application on massively parallel HPC systems. TAU has been successfully applied to a wide range of sub-to-hypersonic flow problems, both in scientific and industrial applications, including the analysis of re-usable launcher configurations (Ecker, 2020; Bykerk et.al., 2020; Bykerk, 2022, 2023). The calculation of the inviscid fluxes in the finite volume framework is based on the application of the AUSMDV flux vector splitting scheme together with MUSCL gradient reconstruction to achieve second order spatial accuracy. Viscous fluxes are treated with a low-dissipation central discretization scheme.

For RANS computations, turbulence was modelled with a Spalart-Allmaras one-equation model, as it provides a good compromise between numerical efficiency and accuracy. This model completely resolves the structure of the turbulent boundary layer including the laminar sub-layer. Thus, an adequate setup of the numerical grid is required which is achieved by using prismatic sub-layers close to the wall with a first dimensionless wall spacing of y^+ of 1 and a wall normal stretching ratio of grid cells of less than 1.3.

Scale-resolving simulations in TAU are conducted using a central discretization scheme with improved dissipation and dispersion (low-dissipation and low-dispersion, LD2) properties (Probst, 2016). Together with various types of Detached Eddy Simulation (DES) models, this scheme has been applied in several studies (see e.g. Schumann (2019)) of launch vehicle aerodynamics. This work uses the iDDES model of Shur (2008) which was designed for better treatment of reattaching turbulent boundary layers. The time accurate simulation in this work use a Jameson-type dual-timestepping approach with a physical time step size of $\Delta t = 2 \times 10^{-6}$ s. In this time-stepping approach, the inner iterations are advanced by a fully-implicit Backward-Euler scheme at a CFL number of 10. Based on the convergence properties of specific integral flow variables, the inner iterations usually converge within 200 steps.

The RANS and iDDES grids both use a spherical domain with approximately 50 rocket lengths upstream and downstream of the vehicle centrepoint. For the RANS mesh, blocks of refinement have been placed around the entire vehicle, as well as in the base region, which can be seen in Figure 3.

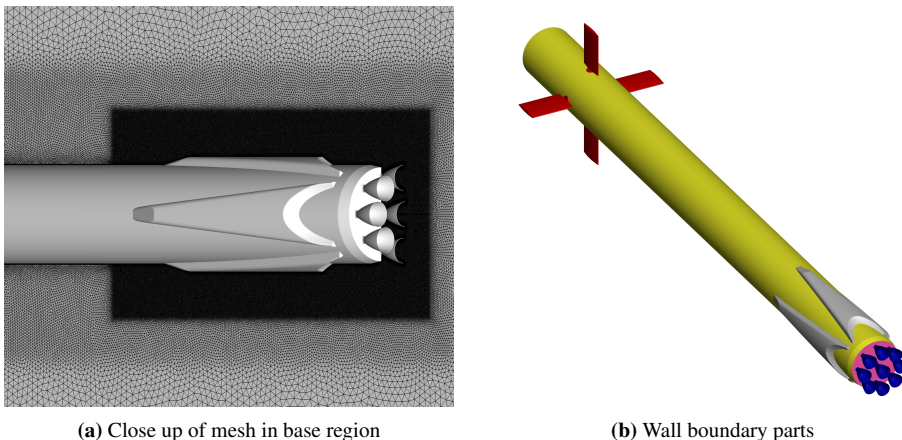


Figure 3. Overview of RANS grid

Here the separate wall boundaries are also shown, with red surfaces for the fins, the wall coloured yellow,

the nozzles denoted by blue, the baseplate shown in pink and the landing legs in grey. Note that the interstage is not visible, but is a cavity which extends internally down to the fins from where the second stage was attached.

A one-eighth domain is used to exploit the vehicle and flow symmetry, with the grid containing approximately 9 million points. For the iDDES computation, a full domain was used with high levels of refinement contained to the base area only, with a total of 31.1 million grid points. A relatively coarse grid has been used away from the landing legs, as the pressure fluctuations on the surface of the landing legs and nozzles were the focal point of this investigation.

5 Results

5.1 RANS results and aerodynamic analysis

Figure 4 presents an annotated overview of Mach contours as the vehicle decelerates from Mach 1.45 down to Mach 0.75. Some typical features of supersonic flows, as well as known trends associated with the transonic regime are observed. These include the presence of a bow shock at supersonic Mach numbers, whose stand off distance increases with decreasing Mach number, until it disappears below Mach 1.

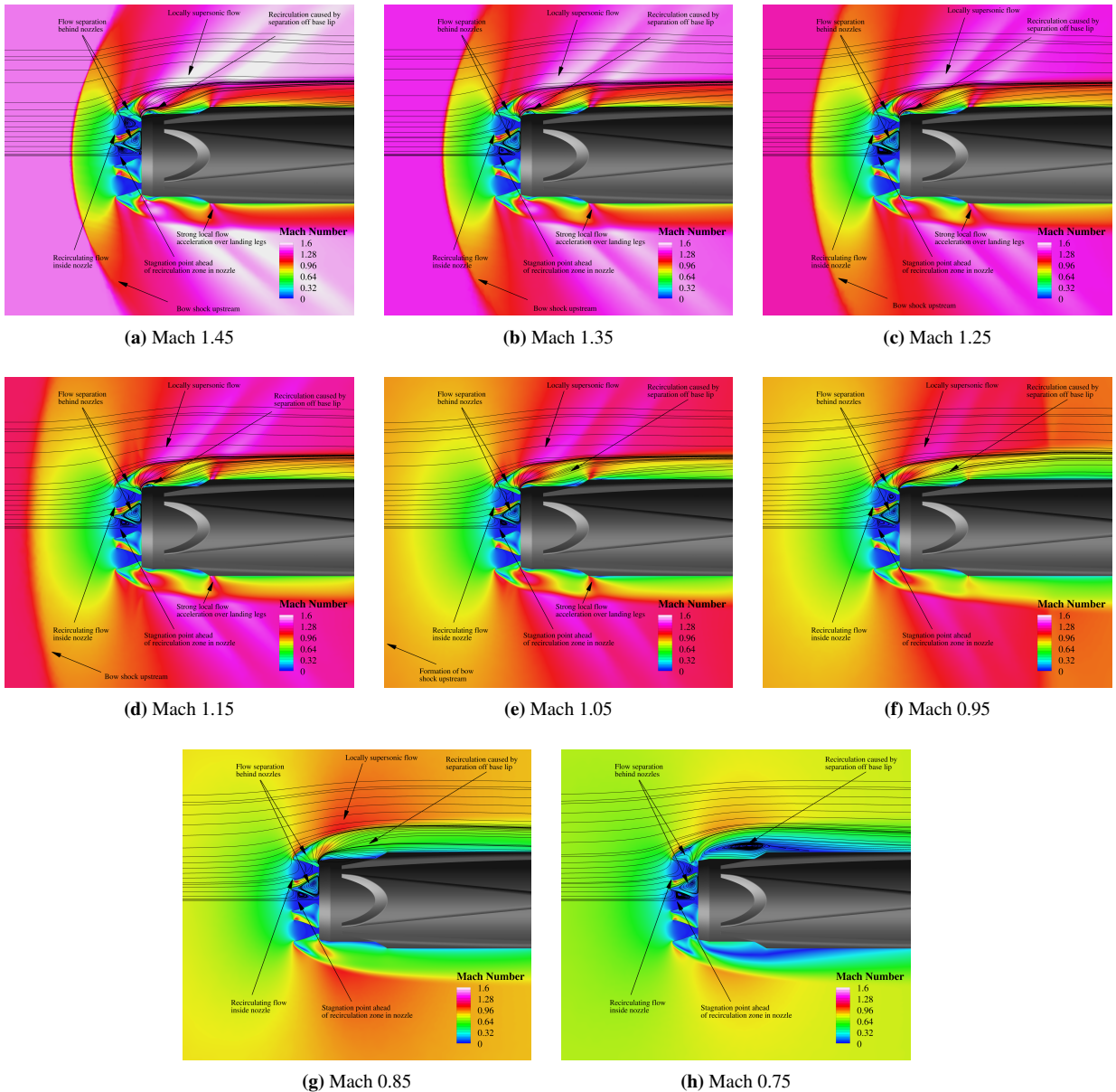


Figure 4. Annotated Mach contours during deceleration from Mach 1.45 to Mach 0.75

At Mach 0.75, a large separation bubble exists as the flow separates off the lip of the baseplate. Above Mach 0.75, the size of the separation bubble is significantly reduced and coincides with supersonic flow occurring

in the vicinity of the landing legs. Locally supersonic flow is also observed at the crotch of the landing leg structure. This is due to the ramp like geometry accelerating the subsonic flow to sonic conditions before expanding over the back side of the landing leg cover. Some features are independent of the freestream Mach number, such as the recirculating flow which is seen inside and around the nozzles. This is because the flow is decelerated as it approaches the base region of the rocket and results in a relatively constant Mach number field, regardless of the freestream velocity. In addition, a free stagnation point exists along the vehicle centreline, where the stagnation streamline meets recirculating flow inside the nozzle.

Figure 5 shows the global drag curve of the RFZ model through the Mach number range investigated. For reference, experimental data for a slender cylinder exposed to an axial flow is also provided (Hoerner, 1965). For the cylinder it is noted that the total drag is dominated by high pressure at the front face due to flow stagnation, with an added contribution from low pressure at the aft face, which is due to flow separation and the resulting wake region. It is clearly shown that the trend of both datasets aligns strongly, highlighting that the drag coefficient of the RFZ model is largely defined by the cylindrical shape of the rocket. The positive drag offset from the basic cylinder is expected and can be attributed to the presence of the fins, nozzles and landing legs.

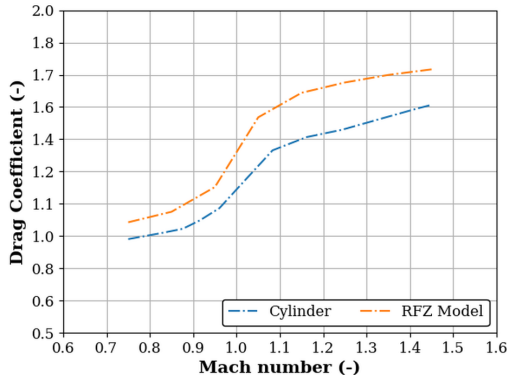


Figure 5. Drag data for a cylinder exposed to an axial flow (Hoerner, 1965) compared with the RFZ model

Table 2 presents a breakdown of drag as per the defined wall boundaries. During deceleration, the interstage and fins experience increasing drag before a peak at Mach 1.15 is reached. As the vehicle continues to decelerate, drag begins to reduce. Other key observations include the minimal and mostly negative drag on the vehicle wall. The wall boundary generally consists of a surface which is parallel to the freestream and as such, is only subjected to viscous drag forces. However, an inclined area does exist at the transition from the baseplate to the body of the rocket, where strong flow acceleration is observed. This leads to a significant low pressure region causing a suction effect. In cases where drag is negative, this suction force overcomes the viscous drag reported at the wall. This explanation is also valid for the legs, where negative drag was also observed below Mach 1.15. It is seen that the drag coefficient associated with the baseplate decreases steadily as the vehicle slows. This is due to decreasing stagnation pressure as well as lower static pressure ratios across the bow shock for cases with a freestream Mach number above 1.

Part	Mach 0.75	Mach 0.85	Mach 0.95	Mach 1.05	Mach 1.15	Mach 1.25	Mach 1.35	Mach 1.45
Legs	-0.084	-0.080	-0.067	-0.016	0.006	0.012	0.019	0.025
Wall	-0.030	-0.032	-0.043	-0.025	-0.009	-0.002	0.002	0.006
Interstage	0.142	0.146	0.161	0.284	0.290	0.284	0.272	0.257
Fins	0.048	0.051	0.100	0.174	0.179	0.175	0.167	0.157
Baseplate	0.039	0.082	0.116	0.202	0.290	0.348	0.397	0.444
Nozzles	0.899	0.896	0.911	0.882	0.860	0.848	0.842	0.837
Total	1.014	1.063	1.178	1.502	1.616	1.664	1.699	1.725

Table 2. Drag coefficient breakdown through transonic regime

While not explicitly shown in the force breakdown, it is worth mentioning that the peripheral nozzles experience larger drag forces than the central nozzle. This is attributed to surface pressures on the outer faces of the nozzles. The central nozzle is immersed in a large recirculation region, which causes the incoming flow to be accelerated and funneled around the peripheral nozzles. This results in lower static pressures acting on the outer faces of the peripheral nozzles compared to the central.

5.2 Numerical Results from the Improved Delayed Detached-Eddy Simulation

This part presents the numerical results of the scale-resolving simulation at $\text{Ma} = 0.85$ and an AoA of 2° . To initiate the iDDES simulation, it was restarted from a converged steady RANS solution using the improved numerical settings listed above. Then, the simulation was continued for 0.311 seconds to establish the resolved turbulent flow field. This amounts to approximately 2 convective time units (CTUs) considering the length of the full vehicle of 47 m. From the simulation results it can be deduced that this is long enough to fully establish the turbulent structures in the launcher base region. The simulation was then continued for another 0.23 seconds where the flow variables were sampled for first- and second-order statistics. Figure 6 shows a qualitative overview of the resolved turbulent vortices in the base plate region using the Q criterion.

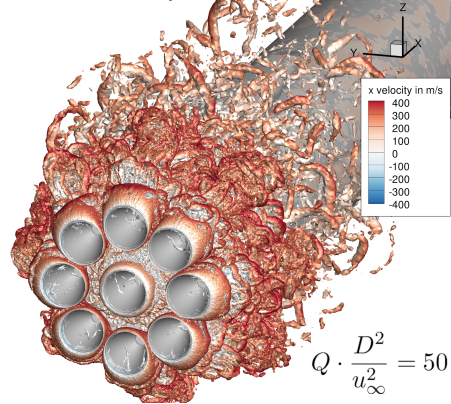


Figure 6. Instantaneous isocontours of the Q-criterion for visualization of the vortical structures around the base region. A non-dimensional value of Q (based on the freestream velocity u_∞ and the vehicle diameter D) of 50 has been chosen. The contours are colored by the local axial flow velocity

These vortices are generated at the sharp edges of the nozzle extensions, forming the separated flow zone near the base plate and the lower bottom of the launcher body. The vortices are convected downstream and impinge partially on the vehicle base plate. It should also be noted that due to the small AoA, also weaker vortices are shed on the inside corner of the nozzle lip. These smaller vortices eventually impinge on the inner part of the nozzle extension but contribute less to the overall unsteady loads on the nozzle structures.

One goal of this study is to evaluate how large the unsteady pressure loads on the surface are, and how they are distributed. This question is addressed by Figure 7 showing the pressure root-mean-square (RMS) distribution on the vehicle surface, normalized by the freestream dynamic pressure p_{dyn} :

$$\frac{p_{\text{RMS}}}{p_{\text{dyn}}} = \frac{\sqrt{\langle (p - \langle p \rangle)^2 \rangle}}{\frac{1}{2} \rho_\infty u_\infty^2} \quad (1)$$

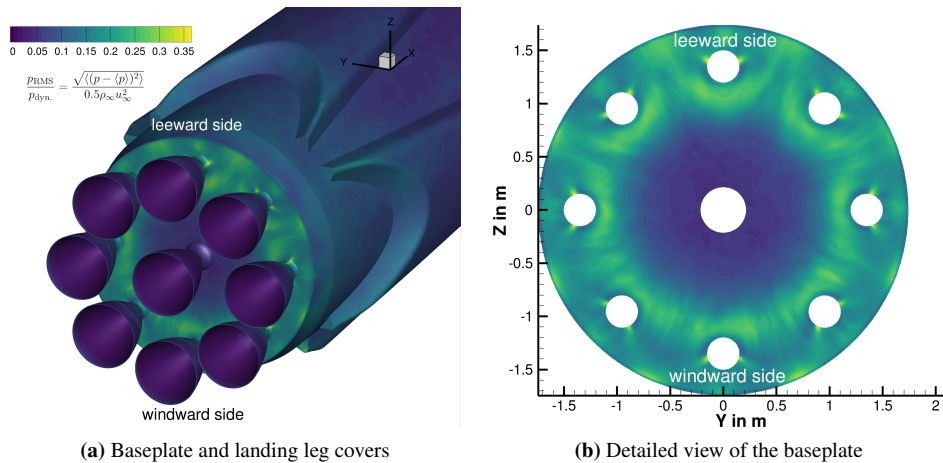


Figure 7. Overview of the RMS pressure fluctuations on the vehicle surface, normalized by the freestream dynamic pressure

Figure 7 highlights that most of the unsteady pressure loads are located on the base plate of the launch vehicle. To better interpret the results, Figure 7 (b) gives an unobstructed view by hiding the exhaust nozzles.

Here, the highest activity reaches 37.2 % of the freestream dynamic pressure, the highest value on the entire vehicle. Vortex shedding by the outer nozzles dominates the spatial distribution of p_{RMS} while no footprint of vortices from the central nozzle is visible on the base plate. This is in agreement with the RANS simulations, where it was noted that a recirculation zone forms around the base of the central nozzle. This constrains the flow and shields the baseplate from direct impingement of shed vortices. Lower unsteady pressure loads are encountered on the interstage section of the vehicle (up to 26.1 %) and on the landing leg covers (up to 28.3 %). Pressure loads on the landing leg covers could, however, be more critical as these are lightweight structures that might be susceptible to unwanted mechanical oscillations.

A more quantitative comparison between the steady RANS and the iDDES results are shown in the Mach number contour plot of Figure 8. The overall structure of the flow fields for both simulations agree very well, especially considering the relatively short sampling time of 1.35 CTU for the iDDES. Small differences persist, however, in the expansion region near the outer nozzles. While the iDDES predicts a clearly separated flow region (dark blue streak), especially on the leeward side, the RANS simulation only shows a very small recirculation zone near the vehicle wall. This good agreement for the time-averaged Mach number also suggests that the overall drag and lift coefficients should be similar for the steady RANS and the time-averaged iDDES simulation.

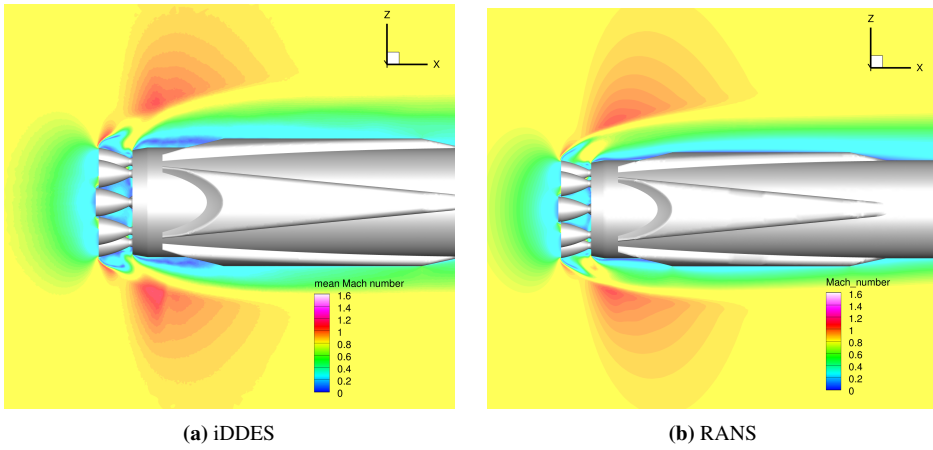


Figure 8. Comparison of the Mach number field between the time-averaged and steady-state results

It was found that even though the lift coefficients obtained from both simulations agree very well (error of 0.5 %), the drag coefficients differ by about 14.4 %. Further analysis of the results showed that this is mainly caused by insufficient mesh refinement at the aft end of the booster. In backward flight, this part of the launch vehicle forms a recirculation zone which is responsible for about 23 % of the vehicle's total drag. As the focus of this iDDES was initially put on the base flow region, grid refinement past the landing leg covers was neglected, which does not allow for a proper scale-resolving simulation. Therefore, an error in drag of about 53 % for this specific boundary part was encountered. Excluding the interstage from the calculation of the vehicle integral drag coefficient, the error between the RANS simulation and the iDDES reduces to about 5 %.

6 Conclusions and future work

This paper has presented results generated using the open-source, common research geometry for re-usable launchers (the RFZ model) in the transonic regime. RANS computations have shown that the trend for drag coefficient agrees well with published results for a basic cylinder placed in an axial flow, where drag is mostly attributed to the high pressure on the surface of the baseplate and the nozzles. Flow separation off the nozzles influences the local flowfield experienced by the landing leg covers, but predominantly affects the pressure loads recorded on the baseplate. This was highlighted by the iDDES simulation, where fluctuations in the pressure about the mean can reach up to 37.2%. Future work will look to investigate any risk of structural excitation of the landing leg covers and nozzles, as well as evaluate the change in vehicle aerodynamics associated with an engine on case at Mach 0.75, which is the starting point of the landing burn. In addition, assessments of the quality of RANS models compared to scale-resolving turbulence models in predicting the vehicle lift and drag coefficient in the transonic regime will also be conducted. This will require a proper meshing strategy for the iDDES simulation, not only for the base flow region, but also in the rear part of the interstage area. Numerical validation will not only rely on the comparison of steady and unsteady methods, but also requires the support of experimentalists through wind tunnel testing campaigns.

References

- Galway, R.D. and Mokry, M., 1977, Wind Tunnel Tests of ONERA Aircraft Models, National Aeronautical Establishment.
- North Atlantic Treaty Organization. Advisory Group for Aeronautical Research and Development, 1958, Wind Tunnel Calibration Models - AGARD Specification 2, NATO.
- Beyers, M. and Huang, X., 1990, Subsonic Aerodynamic Coefficients of the SDM at Angles of Attack up to 90°, NRC, Ottawa, Canada.
- Rivers, M. B., Quest, J., and Rudnik, R., 2015, Comparison of the NASA Common Research Model European Transonic Wind Tunnel Test Data to NASA Test Data (Invited), AIAA SciTech Forum, Kissimmee, Florida, AIAA, January.
- Giannelis, N.F., Bykerk, T., and Vio, G.A., 2023, A Generic Model for Benchmark Aerodynamic Analysis of Fifth-Generation High-Performance Aircraft, *Aerospace*, 10(9), Article 746. URL: <https://www.mdpi.com/2226-4310/10/9/746>, ISSN: 2226-4310.
- Basov, L., Ertl, M., and Bykerk, T., 2024, Comparison of Fokker-Planck and CFD simulations of the RFZ-ST2 upper stage, HiSST: 3rd International Conference on High Speed Vehicle Science and Technology, Busan, Korea, April.
- Ertl, M., and Bykerk, T., 2024, A standard model for the investigation of aerodynamic and aerothermal loads on a re-usable launch vehicle - second stage geometry, HiSST: 3rd International Conference on High Speed Vehicle Science and Technology, Busan, Korea, April.
- Karl, S., Bykerk, T., and Laureti, M., 2024, Design of a truncated ideal nozzle for a re-usable first stage launcher, HiSST: 3rd International Conference on High Speed Vehicle Science and Technology, Busan, Korea, April.
- Bykerk, T., 2023, RFZ Data Repository, URL: <https://zenodo.org/records/8146567>.
- Bykerk, T., 2023, A standard model for the investigation of aerodynamic and aerothermal loads on a re-usable launch vehicle, 10th EUCASS – 9th CEAS Conference 2023, Lausanne, Switzerland, July.
- Ecker, T., Karl, S., Dumont, E., Stappert, S., Krause, D., 2020, "Numerical Study on the Thermal Loads During a Supersonic Rocket Retropropulsion Maneuver," *Journal of Spacecraft and Rockets*, Vol. 57, No. 1.
- Bykerk, T., Karl, S., 2023, "Preparatory CFD Studies for Subsonic Analyses of a Reusable First Stage Launcher during Landing within the RETPRO Project," International Conference on Flight Vehicles, 9th European Conference for Aeronautics and Space Sciences (EUCASS), Lausanne, Switzerland, July.
- Bykerk, T., Kirchheck, D., Karl, S., 2022, "Reconstruction of Wind Tunnel Tests using CFD for a Reusable First Stage during Rocket Retro-Propulsion," International Conference on Flight Vehicles, 9th European Conference for Aeronautics and Space Sciences (EUCASS), Lille, France, July.
- Bykerk, T., Kirchheck, D., Karl, S., 2022, "Condensation Modelling of Expanding Cold Gas Jets during Hypersonic Retro-Propulsion Manoeuvres within the RETPRO Project," 23rd Australasian Fluid Mechanics Conference (AFMC), Sydney, Australia, December.
- Bykerk, T., Kirchheck, D., Karl, S., 2022, "Condensation Modelling of Expanding Cold Gas Jets during Hypersonic Retro-Propulsion Manoeuvres within the RETPRO Project," 23rd Australasian Fluid Mechanics Conference (AFMC), Sydney, Australia, December. Probst, A., Löwe, J., Reuss, S., Knopp, T., 2016, "Scale-Resolving Simulations with a Low-Dissipation Low-Dispersion Second-Order Scheme for Unstructured Flow Solvers," *AIAA Journal*, pp. 1972–2987.
- Shur, M. P., Spalart, P., Strelets, M., Travin, A., 2008, "A Hybrid RANS-LES Approach with Delayed-DES and Wall-Modelled LES Capabilities," *International Journal of Heat and Fluid Flow*, pp. 406–417.
- Schumann, J. E., Hannemann, V., Hannemann, K., 2019, "Investigation of Structured and Unstructured Grid Topology and Resolution Dependence for Scale-Resolving Simulations of Axisymmetric Detaching-Reattaching Shear Layers," *Progress in Hybrid RANS-LES-Modelling*. Springer International Publishing, pp. 169–179.
- Hoerner, S.F., 1965, *Fluid Dynamic Drag: Practical Information on Aerodynamic Drag and Hydrodynamic Resistance*.